ARTICLES
PUBLISHED ONLINE: 22 DECEMBER 2014 | DOI: 10.1038/NMAT4167
nature materials

Impact of mesoscale order on open-circuit voltage in organic solar cells

Carl Poelking[1,2*], Max Tietze[3], Chris Elschner[3], Selina Olthof[4], Dirk Hertel[4], Björn Baumeier[1], Frank Würthner[5], Klaus Meerholz[4], Karl Leo[3] and Denis Andrienko[1*]

Structural order in organic solar cells is paramount: it reduces energetic disorder, boosts charge and exciton mobilities, and assists exciton splitting. Owing to spatial localization of electronic states, microscopic descriptions of photovoltaic processes tend to overlook the influence of structural features at the mesoscale. Long-range electrostatic interactions nevertheless probe this ordering, making local properties depend on the mesoscopic order. Using a technique developed to address spatially aperiodic excitations in thin films and in bulk, we show how inclusion of mesoscale order resolves the controversy between experimental and theoretical results for the energy-level profile and alignment in a variety of photovoltaic systems, with direct experimental validation. Optimal use of long-range ordering also rationalizes the acceptor–donor–acceptor paradigm for molecular design of donor dyes. We predict open-circuit voltages of planar heterojunction solar cells in excellent agreement with experimental data, based only on crystal structures and interfacial orientation.

Performance of organic solar cells relies on strong light absorption, efficient exciton formation, diffusion, dissociation, and drift–diffusion of free charges towards electrodes[1–3]. The efficiency of these processes can be optimized by fine-tuning the underlying molecular structures. The donor–acceptor (DA) or acceptor–donor–acceptor (ADA) molecular architectures[4–7], for example, are typical molecular design patterns targeting the absorption strength of an organic dye. The ADA pattern has been successfully employed in the family of dicyanovinyl-substituted oligothiophenes (DCVnTs)[6]: the methylated derivative DCV5T-Me(3,3) (D5M, see Fig. 1) is world-record holder among evaporated small-molecule donor materials with a disclosed chemical structure, yielding a certified power-conversion efficiency of 8.3% (ref. 8).

Beyond optical tuning, design rules targeting the efficiency of exciton and charge diffusion or exciton splitting are virtually nonexistent, because the underlying microscopic mechanisms are not well understood. Efficient exciton dissociation, for example, has been attributed to the assistance of charge separation by a gradient in the free-energy landscape[9,10], structural heterogeneity as a function of distance to the interface[11], doping and charged defects[12], increase in entropy as the electron and hole move away from the interface[13], formation of hot charge transfer states[14], or long-range tunnelling[15].

Realizing that such design rules would be of great help to synthetic chemists, a whole range of classical, quantum and quantum–classical techniques have been developed to simulate molecular excitations in a realistic explicit environment[10,16–19]. It is therefore an unsettling conclusion if theoretical studies of several of the most efficient systems, DCVnT:C_{60} in particular, predict energy levels that should render the solar cell dysfunctional: neither level bending nor level offset obtained at the donor/acceptor interface promote splitting of geminate hole–electron pairs[20]. On the level of charge energetics, the reason for the exceptional performance of this class of materials, and more generally the ADA architecture, simply eludes rationale. The pronounced negative long-axis quadrupole component that is distinctive of ADA-type materials (Fig. 1) only aggravates what is already problematic on a gas-phase level—namely, the vacuum electron affinity (EA) of the supposed donor D5M falling below the EA of C_{60} (ref. 20). As this puzzle is a matter of interface energetics, it connects with a number of studies that establish links among interface structure, level bending and offset[16,21–26]. It turns out that methods used therein cannot account for the performance of D5M:C_{60} either. At the same time, there is no reason to believe that this material system is exceptional. Rather, inconsistencies revealed for D5M:C_{60} should also afflict other donor/acceptor combinations.

Here, we address these inconsistencies, providing the link between molecular structure, energy landscape of the donor/acceptor interface and open-circuit voltage for various donor architectures, including the ADA pattern. We show that the energy landscape is shaped by mesoscale structural order on a length scale in excess of 100 nm. The associated long-range electrostatic effects not only resolve existing inconsistencies, but also rationalize the high efficiency of D5M:C_{60}.

The newly developed simulation approach provides accurate results for both charge energetics and open-circuit voltages. It is based on a perturbative description of localized excitations (here charges) in their molecular surrounding. The excitation energy is decomposed into an intra- and intermolecular part. The former is given by the gas-phase electron affinity (EA) for electrons (e) or ionization energy (IE) for holes (h). The latter consists of the electrostatic (first-order) and induction (second-order) corrections $\Delta_s^{(1)}$ and $\Delta_s^{(2)}$, where $\Delta_s^{(i)} \equiv W_s^{(i)} - W_n^{(i)}$, with charge state $s \in \{e,h\}$, is calculated with respect to the perturbative contribution $W_n^{(i)}$ to the neutral ($s=n$) ground state[27].

The essence of the computational framework is an appropriate treatment of the long-ranged charge–quadrupole interaction on a mesoscale. In organic semiconductors, the leading multipole

[1]Max Planck Institute for Polymer Research, Ackermannweg 10, 55128 Mainz, Germany. [2]Heidelberg Graduate School of Fundamental Physics, INF 226, 69120 Heidelberg, Germany. [3]Institut für Angewandte Photophysik, George-Bähr-Straße 10, 01062 Dresden, Germany. [4]Physikalische Chemie, Universität zu Köln, Luxemburger Straße 116, 50939 Köln, Germany. [5]Institut für Organische Chemie, Universität Würzburg, Am Hubland, 97074 Würzburg, Germany. *e-mail: carl.poelking@mpip-mainz.mpg.de; denis.andrienko@mpip-mainz.mpg.de

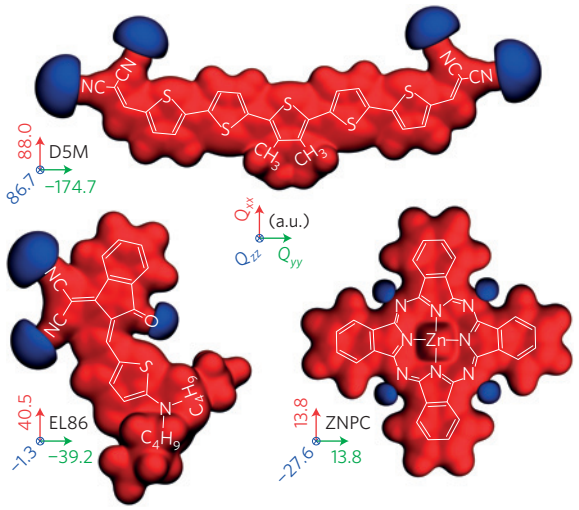

Figure 1 | Electrostatic potential of donor materials. Isosurfaces (blue −1 V, red +1 V) and chemical structures of D5M (ref. 45; ADA architecture), EL86 (ref. 46; DA architecture) and ZNPC. Quadrupole moments are given in atomic units along all three principal axes, as indicated.

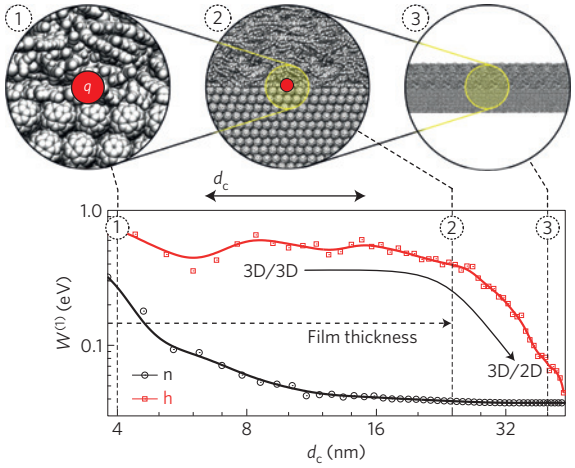

Figure 2 | Convergence of energy levels. Variation of the electrostatic interaction energy $W^{(1)}$ with cluster diameter d_c for a positively charged (h, squares) and neutral (n, circles) DCV4T molecule in a nematically ordered thin film of thickness 12 nm, with solid lines as guides to the eye. Insets 1–3 illustrate the cluster shape and scale at the respective d_c as indicated, with shell-by-shell growth around the central molecular ion q. The crossover from a bulk-like to a slab-like convergence characteristic occurs as $d_c/2$ exceeds the film thickness.

moment in the expansion of the charge density originates from the molecular quadrupole. The charge–quadrupole interaction energy scales as r^{-3} with distance r. Therefore, the energy of a molecular ion embedded in a three-dimensional (3D)-infinite bulk environment is conditionally convergent—that is, can in principle assume any value depending on the surface structure[28]. The situation is mitigated in lower-dimensional systems. Still, in particular in 2D-infinite thin films, the energy convergence is not only slow, but for cluster sizes smaller than the thin-film thickness also passes through a deceptive plateau that resembles the bulk, rather than thin-film energetics. This is illustrated in Fig. 2, where the electrostatic energies for a positively charged and a neutral molecule embedded in a slab of DCV4T:C_{60} of thickness 12 nm are shown as a function of the cluster size d_c. For a hole, this energy contribution is far from converged even for $d_c = 40$ nm. However, with a typical cutoff of 4–8 nm used in simulations, one might interpret the plateau in the 8–20 nm range (0.5 eV) as the site energy of a hole at the interface, whereas the actual converged value for the 2D-infinite system is −0.7 eV.

Even though electrostatic effects in organic semiconductors have been linked to the molecular quadrupole in a variety of theoretical and experimental studies[16,21–26,29–31], the routine use of an interaction range cutoff resulted in a very different and significantly more local interpretation of electrostatic effects. To illustrate how structural coherence fundamentally changes the energy-level profiles, we first compare systems with short- and long-range in-plane molecular order imposed at the D5M/C_{60} interface and subsequently generalize our results to other donor–acceptor heterojunctions.

The position-dependent electrostatic and induction corrections $\Delta^{(1,2)}$ to hole and electron site energies for the D5M:C_{60} system are shown in Fig. 3a,b. Use of a (sizeable) cutoff $r_c = 6$ nm for electrostatics and induction leads to pronounced level bending at the C_{60}/D5M ($z = 0$) and D5M/vacuum ($z = 13$ nm) interfaces (Fig. 3a). The resulting level diagram (Fig. 3c) could give rise to a working solar cell—but only with the roles of donor and acceptor reversed, in clear contradiction to experiments. If we now account for long-range structural order ($r_c = \infty$), the energy landscape changes entirely: Not only does the sign of the offset between donor and acceptor reverse, but the band bending that is present in Fig. 3a is levelled out, as shown in Fig. 3b. The change is mostly due to the electrostatic contribution $\Delta^{(1)}$. It is driven by the competition between in- and out-of-plane interactions that reflect the pronounced quadrupolar and steric anisotropy. Regarding level alignment and profile (Fig. 3d), this solar cell is functional again.

Polarization leads to a further increase of the donor–acceptor offset for hole and electron levels. This increase is due to the build-up of dipole layers across the interface. These have in fact been discussed as contributing to level bending[20,24]. This conclusion applies, however, primarily to the short-range picture: with the long-range correction in place, as Fig. 3d shows, only the C_{60} levels remain slightly bent owing to the interaction of the charge and its polarization cloud with a polarization layer in C_{60}, in line with the step in quadrupolar fields. The donor IE and EA profiles are flat as a result of the large extension of the layer in the xy plane.

Furthermore, the effect of surface quadrupoles has been described in terms of an effective dipole layer, as some of the quadrupolar tensorial components can be represented as two dipoles joined tail to tail[30,31]. This approximation is, however, misguiding, as surface quadrupoles and dipoles promote very different long-range electrostatics owing to their distinct symmetry properties and convergence behaviour. Specifically, quadrupoles alone do not generate a shift of the vacuum level, only dipole layers do.

With the electrostatic and induction contributions taken into account, we can directly test our conclusions against experimental measurements. To this end, we have simulated and measured the ionization energy during stepwise growth of the donor D5M on a C_{60} substrate, see Fig. 4. The measurements, carried out via ultraviolet photoelectron spectroscopy (UPS), indicate a constant IE of 5.75 eV for all thicknesses of the donor film. Simulations also produce a fast convergence to a constant thin-film IE obtained for film thicknesses larger than 1–2 nm (for the comparison, we assumed a penetration depth of two monolayers into the material). Correcting for the vacuum-level shift, which with the method at hand can be probed directly, as well as the internal gas-phase contribution (6.63 eV), an excellent agreement for the D5M IE is achieved between experiment and theory (blue and red horizontal lines in Fig. 4). Both the qualitative and quantitative agreement indicate that electronic levels are indeed determined by long-range electrostatic effects that accompany mesoscale order and secure a flat energy profile within the domains.

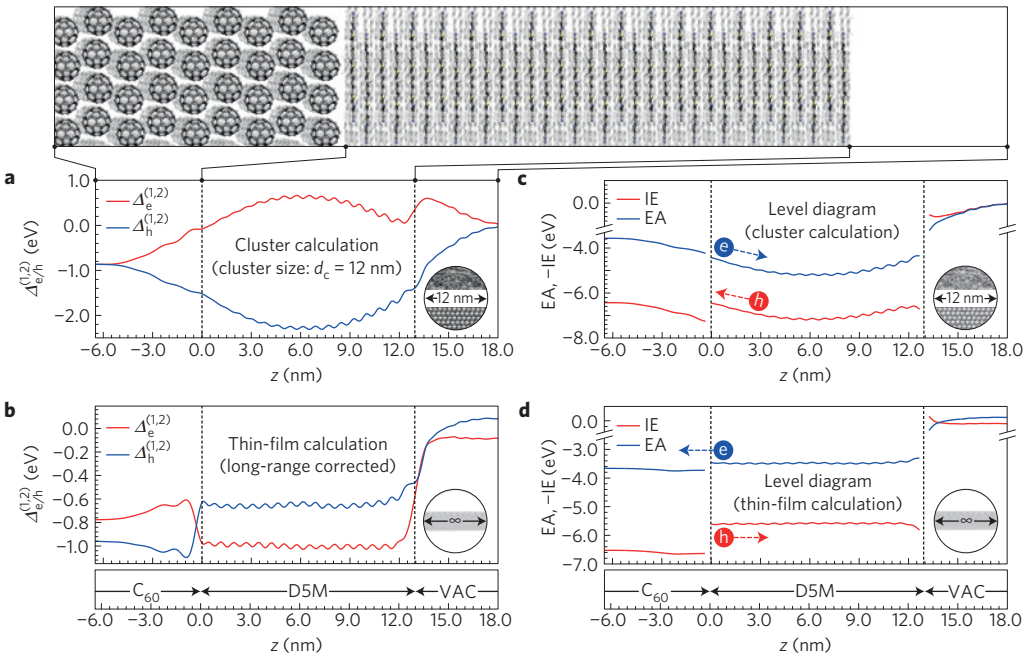

Figure 3 | Hole and electron energy profiles with and without long-range correction. a,**b**, Position-dependent electrostatic and induction contribution $\Delta^{(1,2)}(z)$ to hole (h) and electron (e) site energies for a C_{60}/D5M crystal/crystal interface in the semiconverged regime (**a**) and in the 2D-converged regime with infinite interaction range (**b**). The insets illustrate the system configuration used in the respective computation (spherical cluster or thin film). **c**,**d**, Level diagrams for the two regimes differ qualitatively with respect to level bending and offset. The level alignment obtained for the 12 nm clusters (**c**) leads to trapping of holes at the interface and extraction of electrons towards the donor rather than acceptor. The long-range corrected scenario (**d**) provides flat energy profiles and offsets suited for a functional photovoltaic device (for illustration of gradients, blue circles represent electrons, red circles holes). Note that the cutoff procedure employed in **a**,**c** includes an electrostatic buffer shell that guards against parasitic polarization effects at the cluster edges.

So far, all conclusions have been drawn only on the basis of the D5M:C_{60} system. The physical mechanisms, however, apply to different donor/acceptor combinations in a generic fashion. We first show that other donor materials exhibit the same cluster-size dependence of energy levels that has already been exemplified in Fig. 2. For this purpose we consider thin films of three different donor architectures (D, DA, ADA) and 10 nm thickness, with the molecular ion embedded in the centre of the film. The cluster-size and orientation-dependent contributions $W^{(1)}$ to the absolute state energies (neutral, hole and electron) are shown in Fig. 5a–c. As before, a semiconverged plateau that resembles bulk conditions is observed in the 6–12 nm range, which subsequently splits according to the orientation of the molecules in the thin film. The very slow convergence (which becomes yet slower with increasing film thickness) again hints at the electrostatic competition between in- and out-of-plane charge–quadrupole interactions. As a result, systems with moderate quadrupolar moments such as pentacene exhibit the same qualitative behaviour as the massively quadrupolar ADA compounds.

A direct validation of these simulation results is again possible. Taking into account the full energetic landscape, we arrive at Fig. 6a, which compares calculated and measured thin-film IEs in a device set-up. The set of donor molecules covers a wide spectrum of gas-phase IEs, ranging between 5.2 and 6.8 eV, as well as draws from different molecular design paradigms. Here, each simulated stack consists of 10 nm of the respective donor material on top of 10 nm C_{60}. To address the surface sensitivity of UPS, simulated hole energies are shown as a function of the penetration depth $1/\alpha$. It can be seen that simulation results (blue bars) not only quantitatively reproduce measured trends for the orientation dependence, but also the absolute experimental IE values extracted from UPS (black bars). The largest deviation occurs for pentacene, where UPS measures a larger stabilization than is simulated; this could be due to the enhanced hole delocalization that accompanies the very high charge mobility observed in this compound. Still, even then the molecular orientation can be deduced from a single IE measurement, without laborious structural characterization.

Starting from the single-carrier energy landscape of the planar heterojunctions, we furthermore computed the charge-density-dependent open-circuit voltage. To this end, we additionally took into account thermal disorder[32], which leads to a broadening of the density of states (DOS) around the mean IE and EA even in highly crystalline materials[33]. Thermal effects were simulated via molecular dynamics or estimated from the compound's paracrystallinity (Methods). The resulting distributions of hole energies are approximately Gaussian, with widths (σ) on the order of 30–100 meV obtained for the donor materials studied here (see the inset in Fig. 6b). Assuming sufficiently fast relaxation of charge carriers, this disorder, together with the hole charge density n_h, determines both the transport level located approximately $-\sigma^2/k_BT$ below the mean of the DOS, and the chemical potential μ_h in the donor layer. The electron charge density and chemical potential μ_e on the acceptor side can subsequently be calculated by enforcing charge neutrality in a Fermi–Dirac occupied DOS. We obtain the open-circuit voltage V_{oc} as the difference in chemical potential on the donor and acceptor side, in dependence on the fraction of occupied sites $p = n_h/N_D$ in the donor layer (Fig. 6b), where N_D denotes the donor spatial DOS. The comparison between the computed (red bars) and measured (black bars) open-circuit voltages exhibits excellent agreement within the range of typical charge densities under open-circuit conditions and AM1.5g illumination ($p = 10^{-5}$, corresponding to $n_h \simeq 10^{16}$ cm^{-3}).

Figure 6b also shows photovoltaic gaps Γ as the sum of the mean donor IE and acceptor EA: as the chemical potentials for holes and electrons, μ_e and μ_h, lie fairly deep in the respective DOS, the difference $\Gamma - V_{oc}$ amounts to around 0.6 eV for the

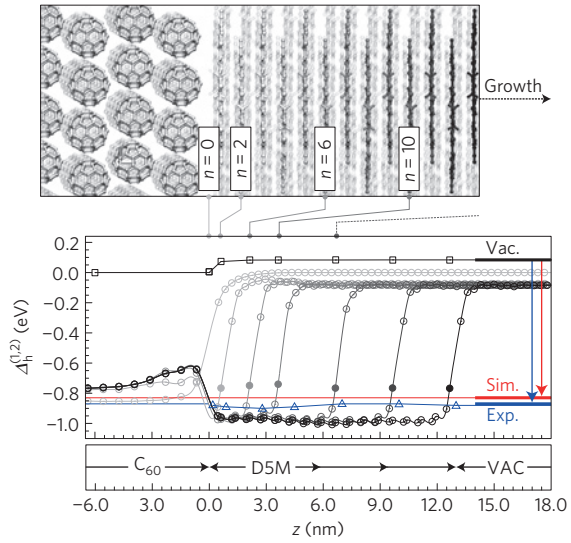

Figure 4 | Evolution of energy profiles and offsets during growth of the donor layer. Energy profiles $\Delta_h^{(1,2)}(z)$ for holes (grey-scaled lines with circles) at various layer thicknesses n of the donor (D5M) layer, ranging from $n=0$ (light grey) to $n=34$ (black) with intermediate steps at $n=2,6,10,18,26$. Solid circles indicate the topmost D5M monolayer. UPS values for $\Delta_h^{(1,2)}$ (blue solid line with triangles) have been calculated by subtracting the gas-phase IE from the measured potentials. In the comparison of the simulated average energy $\Delta_h^{(1,2)}$ (red horizontal line), the vacuum-level shift (line with squares) is taken into account.

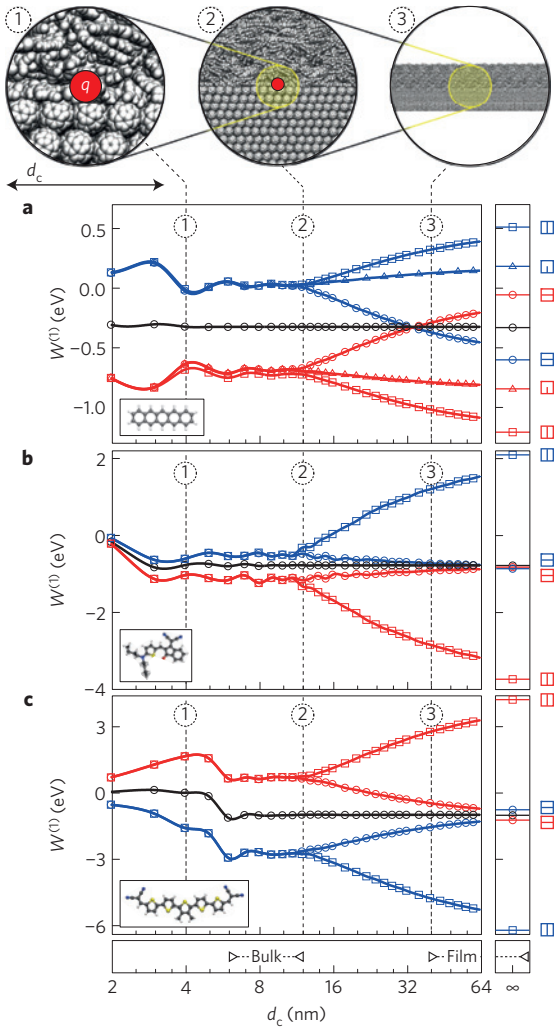

Figure 5 | Convergence of energy levels for pentacene, EL86 and D5M. **a**–**c**, Cluster-size and orientation dependence of the electrostatic interaction energy $W^{(1)}$ in crystalline thin films of 10 nm thickness, composed of three different donor materials: pentacene (D architecture, **a**), EL86 (DA architecture, **b**) and D5M (ADA architecture, **c**). Black, blue and red lines pertain to $W^{(1)}(d_c)$ for the neutral, electron and hole state, respectively. Molecular orientation is indicated by circles (face-on), squares (short-edge-on) and triangles (long-edge-on), as furthermore represented by the cartoons in the rightmost panel: box with horizontal line (face-on), short vertical line (short-edge-on) and long vertical line (long-edge-on). Insets 1–3 illustrate the cluster shape and scale at the respective d_c as indicated, with shell-by-shell growth around the central molecular ion q.

mildly disordered systems (P3HT, sexithiophene, pentacene), but grows considerably with energetic disorder, reaching 0.9 eV for D5M:C_{60}. This finding is supported by a number of studies[32,34,35] where energetic disorder has been hypothesized as a contribution to the observed gap: experimentally, $\Gamma - V_{oc}$ has been located at around 0.5 eV (ref. 34), but a universality to this relationship has been disproved[35]. This apparent universality is due to the influence of thermal motion always being on the same energy scale, k_BT. The resulting thermal disorder strengths are typically smaller than 80 meV (see inset in Fig. 6b)—up to where the chemical potential at open-circuit conditions lies roughly 0.3 eV below the mean of the DOS, leading to an observed gap of twice that amount when accounting for both donor and acceptor.

A more direct comparison between theory and experiment than in Fig. 6b would require the calculation of the illumination-dependent open-circuit voltage, which can be achieved only by explicitly simulating the dynamics of charge generation and recombination[32,36–39]. Targeting the open-circuit voltage as a function of charge density avoids simulation of recombination rates, mobilities and optical profiles. Owing to its simplicity, it provides an equivalent and computationally accessible measure of the energetic capabilities of a donor/acceptor system.

In summary, we have demonstrated how long-range electrostatic effects fostered by mesoscale structural order determine electronic energy levels at organic/organic interfaces. The developed computational framework has been shown to provide accurate results for the energy landscape and open-circuit voltage of a variety of photovoltaic systems.

As a direct consequence of long-range molecular ordering, the simulated energy-level profiles are largely flat, as also probed by UPS measurements. In realistic morphologies, this type of molecular organization can result from extended crystallites forming on the substrate, or simply from preferential alignment of individual molecules induced by the interface in otherwise disordered materials. In fact, anisotropic dielectric properties and, consequently, nematic or smectic ordering are frequently observed in thin organic films[40] and are sufficient to influence the level offset between donor and acceptor domains via uncompensated interface-active quadrupole moments $Q_{20}=Q_{zz}$ and $Q_{22c}\sim Q_{xx}-Q_{yy}$. Structural coherence in the active layer of bulk heterojunctions will differ from the planar set-up, but the nematic (uniaxial) order is retained[40] with the effect that the same energetic mechanisms as for bilayers also apply here. This is supported by the common experimental finding that open-circuit voltages are only slightly larger in the planar layout.

The link between molecular order and energy landscape finally rationalizes the success of the DCVnT series and, more generally, of the acceptor–donor–acceptor design, patented by Heliatek[41]. First, only the face-on orientation on C_{60} provides a level alignment sufficient for charge separation, but not too large to decrease the

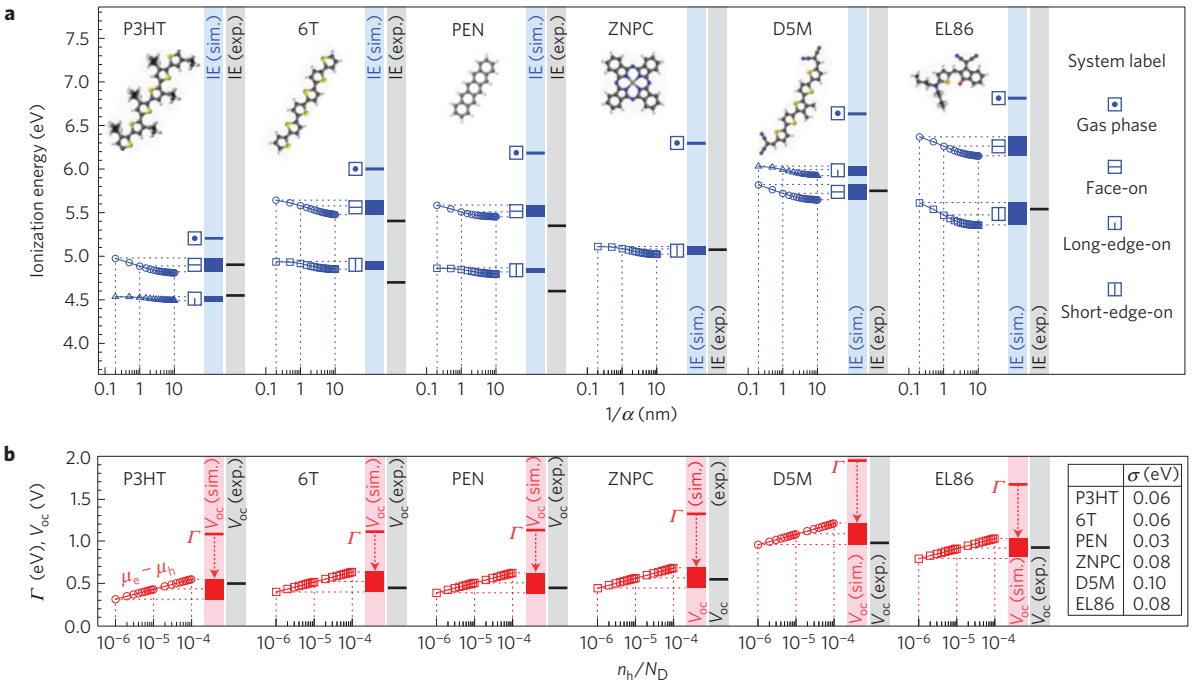

Figure 6 | Ionization energies and open-circuit voltage across different donor/acceptor interfaces. a, Simulated (blue) and experimental (black) ionization energies of different donor materials with molecular structures as shown in the inset. The simulated $1/\alpha$ sampling-depth dependence (blue curves, with dashed lines as guide to the eye) quantifies the reduced dielectric stabilization at the donor/vacuum interface as compared to the donor/acceptor interface, to be taken into account in the comparison with the surface-sensitive UPS technique. Experimental IEs for P3HT, 6T, PEN and ZNPC are taken from refs 31,34,47–49. Gas-phase IEs (blue) were calculated via B3LYP/6-311+g(d,p). **b**, Simulated photovoltaic gap Γ and charge-density-dependent open-circuit voltage V_{oc} (red curves and bars) of the planar heterojunction compared to the experimental V_{oc} (black bars). Line symbols correspond to the configurations from **a**. The calculation of the difference in chemical potential used simulated disorder strengths σ as listed in the inset. The charge-density dependence is expressed in terms of the occupation fraction $p = n_h/N_D$ of donor states. Experimental values for V_{oc} for P3HT, 6T, PEN and ZNPC are taken from refs 34,49,50. All simulated and experimental V_{oc} values apply to the respective planar heterojunction.

open-circuit voltage. Second, with the optical transition dipole moment located in the molecular plane, the face-on orientation ensures efficient light absorption. Third, in this orientation, the π-stacking direction aligns with the interface normal, thus enabling efficient charge transport away from the interface.

This subtle interplay of molecular architecture, orientation, packing and electrostatic effects, that jointly produce a high-performing solar cell, explains why compound design at present is often only rational *ex post*, and why *in silico* screening—for example, using methods as presented here—could be of valuable assistance.

Methods

Computational procedure. The electrostatic first-order and inductive second-order corrections $W_s^{(1)}$ and $W_s^{(2)}$ to charge state ($s \in \{n,e,h\}$) energies are calculated via distributed multipoles $\{Q_{lm}^{as}\}$ of angular momentum lm and polarizabilities $\{\alpha_{lm}^{as}\}$ that are assigned to the set of (atomic) expansion sites $\{a\}$ for each molecule to reproduce the system charge density ρ and linear field response. On this atomistic scale, Poisson's equation $\nabla(\varepsilon\nabla\phi) \sim \rho$ has the variational analogue[27]

$$\delta(W_s^{(1)} + W_s^{(2)})/\delta(\Delta Q_{lm}^{as}) = 0 \qquad (1)$$

and its solution consists of the set of dipolar moments $\{\Delta Q_{lm}^{as}\}$ for each atomic site a of the system, induced in response to the permanent moments $\{Q_{lm}^{as}\}$ that approximate ρ. Note that $W_s^{(1)}$ can be calculated directly from $\{Q_{lm}^{as}\}$, whereas $W_s^{(2)}$ follows only from the solution of equation (1) for all charge states $s \in \{n,e,h\}$.

The molecular electrostatic fields in the neutral and charged states were parametrized via a distributed multipole analysis[42], which derives multipole moments from the density matrix. In the expansion of these fields, we included atom-centred multipoles of rank $l \leq 2$. To describe the molecular field response, we used the Thole model, which damps short-range dipole–dipole interactions to avoid an unphysical overpolarization[43].

An outline of how equation (1) is solved for aperiodic excitations embedded in a periodic background is given in the Supplementary Information. The approach has been implemented in the VOTCA package[17], which is open-source and available online.

Interfaces between C_{60} and P3HT, sexithiophene, pentacene, ZNPC, D5M and EL86 were assembled from the crystal structures of the respective components: the C_{60} exposes its more homogeneous face-centered cubic [111] surface to the donor, whose X-ray crystal structures we cleaved to obtain the desired orientation on the C_{60} substrate. The mismatch between the crystal faces was corrected by a short equilibration of the C_{60} using molecular dynamics. The molecular electrostatic fields in the neutral and charged states were parametrized via a distributed multipole analysis[42], which derives atomistic multipole moments directly from the density matrix. Local atom-centred polarizabilities were adapted from the set of Thole polarizabilities[44] to reproduce the volume of the quantum-mechanically calculated molecular polarizability ellipsoid. Disorder strengths σ were calculated using classical force fields for P3HT, D5M and EL86. For pentacene and ZNPC, in the absence of tailored force fields, disorder was simulated by imposing paracrystalline disorder of $g = 3\%$ and $g = 5\%$, respectively, on the molecular coordinates. Chemical potentials are computed by imposing Fermi–Dirac occupation of the simulated DOS in a charge-neutral system. In this calculation, the EA of C_{60} at -3.7 eV accounts for the enhanced delocalization of the electron, yielding, in dependence on the donor material with spatial DOS N_D, a charge-density-dependent Fermi level between -3.9 eV and -4.1 eV.

Experimental procedure. The UPS samples are thermally evaporated at room temperature under high-vacuum conditions (base pressure $< 1 \times 10^{-8}$ mbar). As substrate, a sputter-cleaned gold foil (99.995%, MaTecK) is used. The donor material DCV5T-Me(3,3) (Synthon Chemicals) is used as delivered, whereas C_{60} (Creaphys) is of fourfold sublimed purity grade. The sample stack Au/C_{60}(5 nm)/DCV5T-Me(3,3) (0.2/0.4/0.9/1.4/2.8/4.5/7.0/10/15/20 nm)/C_{60} (5 nm) is evaporated and measured stepwise. The UPS experiments are performed with a Phoibos 100 system (Specs) at a base pressure of 1×10^{10} mbar directly connected to the evaporation tool. The energy resolution of UPS (HeI, 21.22 eV, sample bias 8 V) is 130 meV. The experimental error (reproducibility) is estimated to 50 meV. For each spectrum, the high binding energy cutoff (HBEC), E_{HBEC}, as well as the HOMO onset of the occupied states, E_{HOMO}, are determined. The film work function is given by $Wf = 21.22\,eV - E_{HBEC}$ and the ionization

energy by IE = Wf + E_{HOMO}. The UPS measurements are performed in the dark to avoid parasitic absorption effects.

Received 30 January 2014; accepted 5 November 2014; published online 22 December 2014

References

1. Brédas, J-L., Norton, J. E., Cornil, J. & Coropceanu, V. Molecular understanding of organic solar cells: The challenges. *Acc. Chem. Res.* **42,** 1691–1699 (2009).
2. Clarke, T. M. & Durrant, J. R. Charge photogeneration in organic solar cells. *Chem. Rev.* **110,** 6736–6767 (2010).
3. Dou, L. *et al.* 25th anniversary article: A decade of organic/polymeric photovoltaic research. *Adv. Mater.* **25,** 6642–6671 (2013).
4. Boudreault, P-L. T., Najari, A. & Leclerc, M. Processable low-bandgap polymers for photovoltaic applications. *Chem. Mater.* **23,** 456–469 (2010).
5. Sommer, M., Hüttner, S. & Thelakkat, M. Donor–acceptor block copolymers for photovoltaic applications. *J. Mater. Chem.* **20,** 10788–10797 (2010).
6. Mishra, A. & Bäuerle, P. Small molecule organic semiconductors on the move: Promises for future solar energy technology. *Angew. Chem. Int. Ed.* **51,** 2020–2067 (2012).
7. Liu, Y. *et al.* Solution-processed small-molecule solar cells: Breaking the 10% power conversion efficiency. *Sci. Rep.* **3,** 3356 (2013).
8. Meerheim, R., Körner, C. & Leo, K. Highly efficient organic multi-junction solar cells with a thiophene based donor material. *Appl. Phys. Lett.* **105,** 063306 (2014).
9. Wilke, A. *et al.* Electric fields induced by energy level pinning at organic heterojunctions. *Appl. Phys. Lett.* **98,** 123304 (2011).
10. Beljonne, D. *et al.* Electronic processes at organic–organic interfaces: Insight from modeling and implications for opto-electronic devices. *Chem. Mater.* **23,** 591–609 (2011).
11. McMahon, D. P., Cheung, D. L. & Troisi, A. Why holes and electrons separate so well in polymer/fullerene photovoltaic cells. *J. Phys. Chem. Lett.* **2,** 2737–2741 (2011).
12. Liu, A. *et al.* Control of electric field strength and orientation at the donor–acceptor interface in organic solar cells. *Adv. Mater.* **20,** 1065–1070 (2008).
13. Gregg, B. A. Entropy of charge separation in organic photovoltaic cells: The benefit of higher dimensionality. *J. Phys. Chem. Lett.* **2,** 3013–3015 (2011).
14. Jailaubekov, A. E. *et al.* Hot charge-transfer excitons set the time limit for charge separation at donor/acceptor interfaces in organic photovoltaics. *Nature Mater.* **12,** 66–73 (2013).
15. Caruso, D. & Troisi, A. Long-range exciton dissociation in organic solar cells. *Proc. Natl Acad. Sci. USA* **109,** 13498–13502 (2012).
16. Yost, S. R., Wang, L-P. & Van Voorhis, T. Molecular insight into the energy levels at the organic donor/acceptor interface: A quantum mechanics/molecular mechanics study. *J. Phys. Chem. C* **115,** 14431–14436 (2011).
17. Rühle, V. *et al.* Microscopic simulations of charge transport in disordered organic semiconductors. *J. Chem. Theory Comput.* **7,** 3335–3345 (2011).
18. Fu, Y-T., Risko, C. & Brédas, J-L. Intermixing at the pentacene-fullerene bilayer interface: A molecular dynamics study. *Adv. Mater.* **25,** 878–882 (2013).
19. Muccioli, L. *et al.* Supramolecular organization of functional organic materials in the bulk and at organic/organic interfaces: A modeling and computer simulation approach. *Top. Curr. Chem.* **352,** 39–101 (2014).
20. Mothy, S. *et al.* Tuning the interfacial electronic structure at organic heterojunctions by chemical design. *J. Phys. Chem. Lett.* **3,** 2374–2378 (2012).
21. Verlaak, S. *et al.* Electronic structure and geminate pair energetics at organic–organic interfaces: The case of pentacene/C60 heterojunctions. *Adv. Funct. Mater.* **19,** 3809–3814 (2009).
22. Linares, M. *et al.* On the interface dipole at the pentacene-fullerene heterojunction: A theoretical study. *J. Phys. Chem. C* **114,** 3215–3224 (2010).
23. May, F., Baumeier, B., Lennartz, C. & Andrienko, D. Can lattice models predict the density of states of amorphous organic semiconductors? *Phys. Rev. Lett.* **109,** 136401 (2012).
24. Idé, J. *et al.* Interfacial dipole and band bending in model pentacene/C60 heterojunctions. *Int. J. Quantum Chem.* **113,** 580–584 (2013).
25. Yost, S. R. & Van Voorhis, T. Electrostatic effects at organic semiconductor interfaces: A mechanism for "cold" exciton breakup. *J. Phys. Chem. C* **117,** 5617–5625 (2013).
26. Idé, J. *et al.* Charge dissociation at interfaces between discotic liquid crystals: The surprising role of column mismatch. *J. Am. Chem. Soc.* **136,** 2911–2920 (2014).
27. Stone, A. J. *The Theory of Intermolecular Forces* (Clarendon Press, 1997).
28. De Leeuw, S. W., Perram, J. W. & Smith, E. R. Simulation of electrostatic systems in periodic boundary conditions. i. lattice sums and dielectric constants. *Proc. R. Soc. Lond. A* **373,** 27–56 (1980).
29. Chen, W., Qi, D-C., Huang, H., Gao, X. & Wee, A. T. S. Organic–organic heterojunction interfaces: Effect of molecular orientation. *Adv. Funct. Mater.* **21,** 410–424 (2011).
30. Heimel, G., Salzmann, I., Duhm, S. & Koch, N. Design of organic semiconductors from molecular electrostatics. *Chem. Mater.* **23,** 359–377 (2011).
31. Duhm, S. *et al.* Orientation-dependent ionization energies and interface dipoles in ordered molecular assemblies. *Nature Mater.* **7,** 326–332 (2008).
32. Garcia-Belmonte, G. & Bisquert, J. Open-circuit voltage limit caused by recombination through tail states in bulk heterojunction polymer-fullerene solar cells. *Appl. Phys. Lett.* **96,** 113301 (2010).
33. Schrader, M. *et al.* Comparative study of microscopic charge dynamics in crystalline acceptor-substituted oligothiophenes. *J. Am. Chem. Soc.* **134,** 6052–6056 (2012).
34. Wilke, A. *et al.* Correlation between interface energetics and open circuit voltage in organic photovoltaic cells. *Appl. Phys. Lett.* **101,** 233301 (2012).
35. Widmer, J., Tietze, M., Leo, K. & Riede, M. Open-circuit voltage and effective gap of organic solar cells. *Adv. Funct. Mater.* **23,** 5814–5821 (2013).
36. Koster, L. J. A., Mihailetchi, V. D., Ramaker, R. & Blom, P. W. M. Light intensity dependence of open-circuit voltage of polymer:Fullerene solar cells. *Appl. Phys. Lett.* **86,** 123509 (2005).
37. Potscavage, W. J., Sharma, A. & Kippelen, B. Critical interfaces in organic solar cells and their influence on the open-circuit voltage. *Acc. Chem. Res.* **42,** 1758–1767 (2009).
38. Vandewal, K., Tvingstedt, K., Gadisa, A., Inganäs, O. & Manca, J. V. On the origin of the open-circuit voltage of polymer–fullerene solar cells. *Nature Mater.* **8,** 904–909 (2009).
39. Maurano, A. *et al.* Recombination dynamics as a key determinant of open circuit voltage in organic bulk heterojunction solar cells: A comparison of four different donor polymers. *Adv. Mater.* **22,** 4987–4992 (2010).
40. Wynands, D. *et al.* Spectroscopic ellipsometry characterization of vacuum-deposited organic films for the application in organic solar cells. *Org. Electron.* **13,** 885–893 (2012).
41. Pfeiffer, M. *et al.* Organic photoactive device. US patent 8426727 (2013).
42. Stone, A. J. Distributed multipole analysis: Stability for large basis sets. *J. Chem. Theory Comput.* **1,** 1128–1132 (2005).
43. Thole, B. Molecular polarizabilities calculated with a modified dipole interaction. *Chem. Phys.* **59,** 341–350 (1981).
44. Van Duijnen, P. T. & Swart, M. Molecular and atomic polarizabilities: Thole's model revisited. *J. Phys. Chem. A* **102,** 2399–2407 (1998).
45. Fitzner, R. *et al.* Correlation of π-conjugated oligomer structure with film morphology and organic solar cell performance. *J. Am. Chem. Soc.* **134,** 11064–11067 (2012).
46. Bürckstümmer, H. *et al.* Efficient solution-processed bulk heterojunction solar cells by antiparallel supramolecular arrangement of dipolar donor–acceptor dyes. *Angew. Chem. Int. Ed.* **50,** 11628–11632 (2011).
47. Zhang, F. *et al.* Energy level alignment and morphology of interfaces between molecular and polymeric organic semiconductors. *Org. Electron.* **8,** 606–614 (2007).
48. Heimel, G. & Koch, N. in *Interface Controlled Organic Thin Films* Vol. 129 (eds Al-Shamery, K., Horowitz, G., Sitter, H. & Rubahn, H-G.) 141–145 (Springer, 2009).
49. Tietze, M. L. *et al.* Correlation of open-circuit voltage and energy levels in zinc-phthalocyanine: C_{60} bulk heterojunction solar cells with varied mixing ratio. *Phys. Rev. B* **88,** 085119 (2013).
50. Kinoshita, Y., Hasobe, T. & Murata, H. Controlling open-circuit voltage of organic photovoltaic cells by inserting thin layer of Zn–phthalocyanine at pentacene/C_{60} interface. *Jpn. J. Appl. Phys.* **47,** 1234–1237 (2008).

Acknowledgements

This work has been supported by the BMBF programme MEDOS (FKZ 03EK3503B). We are grateful to T. Bereau for critical reading of the manuscript and P. Bäuerle and C. Körner for fruitful collaborations.

Author contributions

C.P., B.B. and D.A. conceived and performed simulations. M.T., C.E. and K.L. contributed experimental results on DCVnTs. S.O., D.H., F.W. and K.M. contributed experimental results on merocyanines. C.P. and D.A. wrote the paper.

Additional information

Supplementary information is available in the online version of the paper. Reprints and permissions information is available online at www.nature.com/reprints. Correspondence and requests for materials should be addressed to C.P. or D.A.

Competing financial interests

The authors declare no competing financial interests.